

# <sup>1</sup> DuoDIC: 3D Digital Image Correlation in MATLAB

<sup>2</sup> **Dana Solav<sup>\*1</sup> and Asaf Silverstein<sup>1</sup>**

<sup>3</sup> **1 Faculty of Mechanical Engineering, Technion, Haifa, Israel**

**DOI:** [10.21105/joss.0XXXX](https://doi.org/10.21105/joss.0XXXX)

## Software

- [Review ↗](#)
- [Repository ↗](#)
- [Archive ↗](#)

**Editor:** [Editor Name ↗](#)

**Submitted:** 01 January XXXX

**Published:** 01 January XXXX

## License

Authors of papers retain copyright and release the work under a Creative Commons Attribution 4.0 International License ([CC BY 4.0](#)).

## <sup>4</sup> Summary

<sup>5</sup> Three-dimensional Digital Image Correlation (3D-DIC) is a non-contact optical-numerical  
<sup>6</sup> technique for measuring the 3D shape and full-field displacement, deformation, and strain,  
<sup>7</sup> from stereo digital images of the surface of an object. 3D-DIC is useful in numerous applica-  
<sup>8</sup> tions, such as characterizing the mechanical behavior of materials and structures, quantifying  
<sup>9</sup> material parameters, and validating numerical simulations.

<sup>10</sup> DuoDIC is a freely available open source MATLAB toolbox for 2-camera stereo 3D-DIC,  
<sup>11</sup> which can be used either as a standalone package or as functions in custom scripts. DuoDIC  
<sup>12</sup> receives two series of synchronized images taken from two cameras: (1) images of a flat  
<sup>13</sup> checkerboard target, which are used to calibrate the stereo camera pair; and (2) images of a  
<sup>14</sup> speckled test object, which may undergo movement and deformation. The toolbox processes  
<sup>15</sup> the image series and integrates several camera calibration algorithms with the 2D subset-  
<sup>16</sup> based DIC software Ncorr (Blaber et al., 2015), to transform matching image points into  
<sup>17</sup> 3D points, and outputs a dynamic point cloud, meshed surfaces, rigid body motion, and full-  
<sup>18</sup> field displacement, deformation, and strain measures. Furthermore, DuoDIC offers advanced  
<sup>19</sup> functions to visualize various measures on the 3D meshes and overlaid on the original images.

<sup>20</sup> The simple user interface allows novice users to perform 3D-DIC analyses without interacting  
<sup>21</sup> with MATLAB syntax, while stand-alone functions can be integrated in custom scripts by  
<sup>22</sup> more proficient MATLAB users. As such, DuoDIC is suitable for students, researchers, and  
<sup>23</sup> professionals in various fields.

<sup>24</sup> The package is composed of four main scripts: (1) stereo camera calibration; (2) image cross-  
<sup>25</sup> correlation (2D-DIC); (3) 3D reconstruction; and (4) post-processing. This paper describes  
<sup>26</sup> the algorithms implemented in each step and demonstrates its performance in two test cases,  
<sup>27</sup> which are also included as sample data: rigid body translations of a cylindrical container and  
<sup>28</sup> uniaxial tension of a rubber dog-bone specimen.

## <sup>29</sup> Statement of need

<sup>30</sup> 3D-DIC is useful in numerous applications where the full-field displacements and strains are  
<sup>31</sup> required, primarily for measuring the mechanical response of materials and structures and for  
<sup>32</sup> characterizing mechanical properties, with widespread applications from nano- to macro-scale,  
<sup>33</sup> and rapid progress and developments Pan (2018). 3D-DIC is preferable over strain gages and  
<sup>34</sup> extensometers due to its non-contact nature and the large amount of local information that  
<sup>35</sup> can be collected.

<sup>36</sup> Commercial 3D-DIC software are typically expensive, proprietary and closed-source, which  
<sup>37</sup> may pose a barrier, especially for students and researchers. Notable free and open-source  
<sup>38</sup> 3D-DIC contributions include DICe (Turner, 2015), MultiDIC (Solav et al., 2018), and A

---

\*corresponding author

39 DIC3D (Atkinson & Becker, 2021). Each of these packages uses different algorithms for  
40 correlation and stereo calibration and requires different calibration targets. Specifically, our  
41 previous toolbox MultiDIC focused on multi-view applications, therefore required a non-  
42 planar calibration object, which is relatively difficult to make accurate, thus preventing easy  
43 implementation. To this end, DuoDIC enables a simpler calibration procedure that requires  
44 only a flat checkerboard pattern. In addition, with respect to MultiDIC we improved the post-  
45 processing and visualization options. DuoDIC is written in MATLAB, providing the flexibility  
46 and simple implementation of a high-level language, which meets the needs of the experimental  
47 mechanics community. Moreover, a main advantages of open-source software is the ability  
48 to compare results and performance, and to cross-validate the implementation of different  
49 algorithms and approaches. To this end, DuoDIC may also comprise a complementary tool for  
50 researchers in the field.

## 51 **Algorithms and workflow**

52 The entire 3D-DIC procedure in DuoDIC is organized in four main scripts, which the user can  
53 run without having to interact with any MATLAB syntax. [Figure 1](#) outlines the workflow of the  
54 3D-DIC procedure. The functionality and algorithms incorporated in each step are detailed in  
55 the sub-sections below. The figures in this section represent sample data, which are provided  
56 with the toolbox. The experimental setup used for taking these images consisted of two  
57 machine-vision cameras (BFS-U3-51S5M-C, FLIR, USA), each equipped with a 5.0 MP Sony  
58 IMX250 monochrome sensor and a 25 mm lens (Fujinon HF25SA-1, Fujifilm Corporation,  
59 Japan). The cameras were synchronously hardware-triggered using a MatchID Triggerbox  
60 (MatchID, Belgium). A rubber dog-bone specimen, cut out of a bicycle tube, was mounted  
61 on an optical table (Thorlabs, USA), such that its left end was fixed and its right end was  
62 moved to the right in 19 steps with 1 mm increments, such that A total of 20 images were  
63 taken from each camera (one reference state and 19 deformed states).

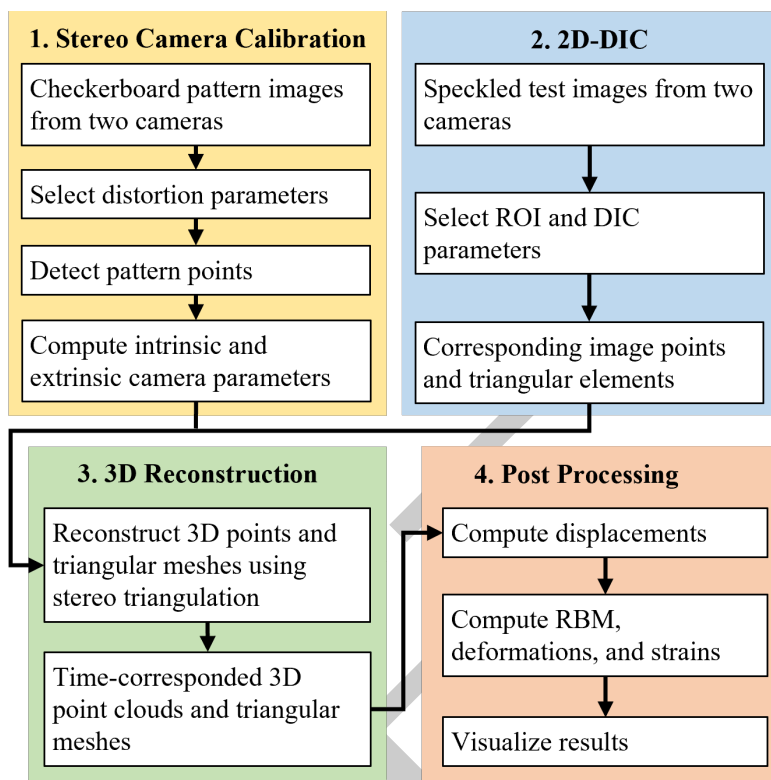


**Figure 1:** DuoDIC algorithm workflow. Each color represent one main script

### Step 1: Stereo camera calibration

In this step, the intrinsic and extrinsic parameters of both cameras are computed by integrating functions from MathWorks Computer Vision Toolbox, which implement algorithms by Zhang (Zhang, 2000), Heikkila and Silven (Heikkila & Silven, 1997), Bouguet (Bouguet, 2013), and Bradski and Kaehler (Bradski & Kaehler, 2008). This script takes as input multiple simultaneous images of a checkerboard target captured by two cameras in a stereo pair. The checkerboard pattern points in each image are automatically detected and used for calibrating the cameras' intrinsic and extrinsic parameters. The intrinsic parameters include focal lengths, principal point (optical center), and up to 6 distortion coefficients. The user can choose between [0,2,3] radial distortion coefficients, [0,2] tangential distortion coefficients, and [0,1] skew parameter. The extrinsic (stereo) camera parameters comprise the 3D position and orientation of the second camera with respect to the first (a total of 6 degrees of freedom). Furthermore, the computed camera parameters are used for computing the reprojection errors, which represent the distance between the reprojected and the detected pattern points, and comprise the accuracy of the estimated camera parameters. An example of the results, which are presented at the end of this step is shown in [Figure 2](#). This calibration was obtained using 52 stereo images of a pattern with a square size of 10 mm, which are included in the sample data provided with the toolbox.

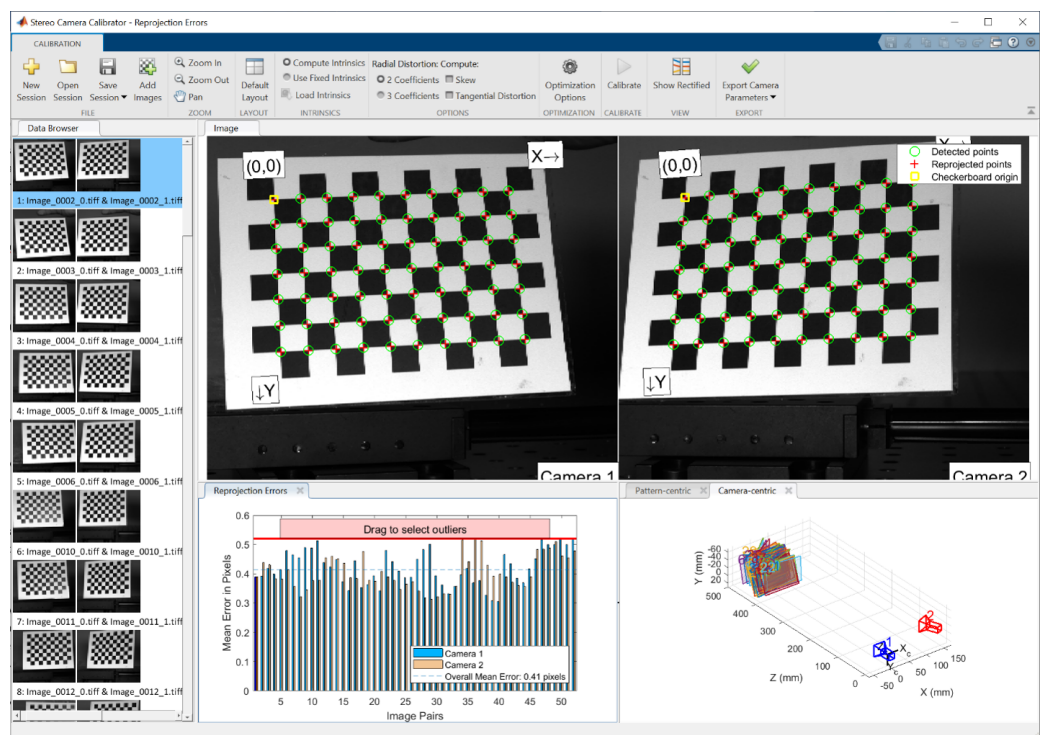


**Figure 2:** Stereo Calibration results. The top panels show the detected and reprojected points for a pair of stereo images. The bottom left panel shows the mean reprojection error for all pairs of images, and the bottom right panel shows the estimated positions and orientations of the cameras with respect to the checkerboard pattern images.

## Step 2: Image cross-correlation (2D-DIC)

In this step, the script receives multiple images of a speckled test object captured simultaneously by the stereo camera pair. Typically, the first pair of images represents the unloaded, or undeformed, configuration and the rest of the images represent deformed states. Ncorr toolbox (Blaber et al., 2015) is utilized in this step to detect a dense grid of matching points on all images. Although Ncorr was created as a 2D-DIC toolbox, typically receiving images from a single camera, DuoDIC utilizes it to detect matching points on images taken from two different views. The images from both cameras in all states are then cross-correlated with the reference image, to detect corresponding points in the selected region of interest (ROI), as demonstrated in Figure 3. For interpreting the values of the correlation coefficients, refer to (Blaber et al., 2015) and (Solav et al., 2018). Furthermore, the point grid is meshed with triangular elements, which are later used in Step 4 for calculating the deformation and strain measures.

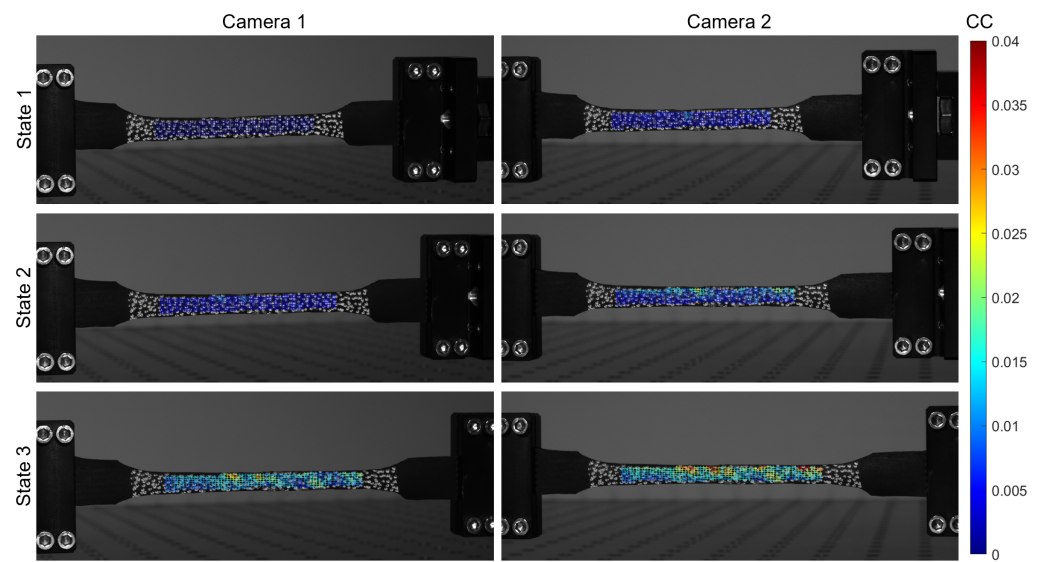


**Figure 3:** Image point matching computed using Ncorr and DuoDIC. The grid of corresponding matched points are plotted with crosses overlaid on each image, with color representing their correlation coefficient (CC) with the reference image (camera 1, state 1, top left panel).

### 95 Step 3: 3D reconstruction

96 The results from Step 1 and Step 2 are combined in this step to obtain the 3D position of  
 97 each image point using stereo triangulation. The set of matching points on each pair of  
 98 stereo images (as computed in Step 2) are first being undistorted using the intrinsic camera  
 99 parameters of each camera, according to the distortion model selected in Step 1. Consequently,  
 100 the image points are transformed into 3D world points using the stereo camera parameters  
 101 computed in Step 1. In addition, the reprojection errors are obtained for each point, by  
 102 calculating the distance (in pixels) between the detected and the reprojected points. At the  
 103 end of this step, the 3D point cloud and triangulated surface are plotted and animated, utilizing  
 104 function from the GIBBON toolbox (Moerman, 2018). Two animated figures plot the values  
 105 of the matching correlation coefficient and the reprojection errors, as shown in [Figure 4](#) for  
 106 the last image in the series, which represents the configuration with the largest stretch.

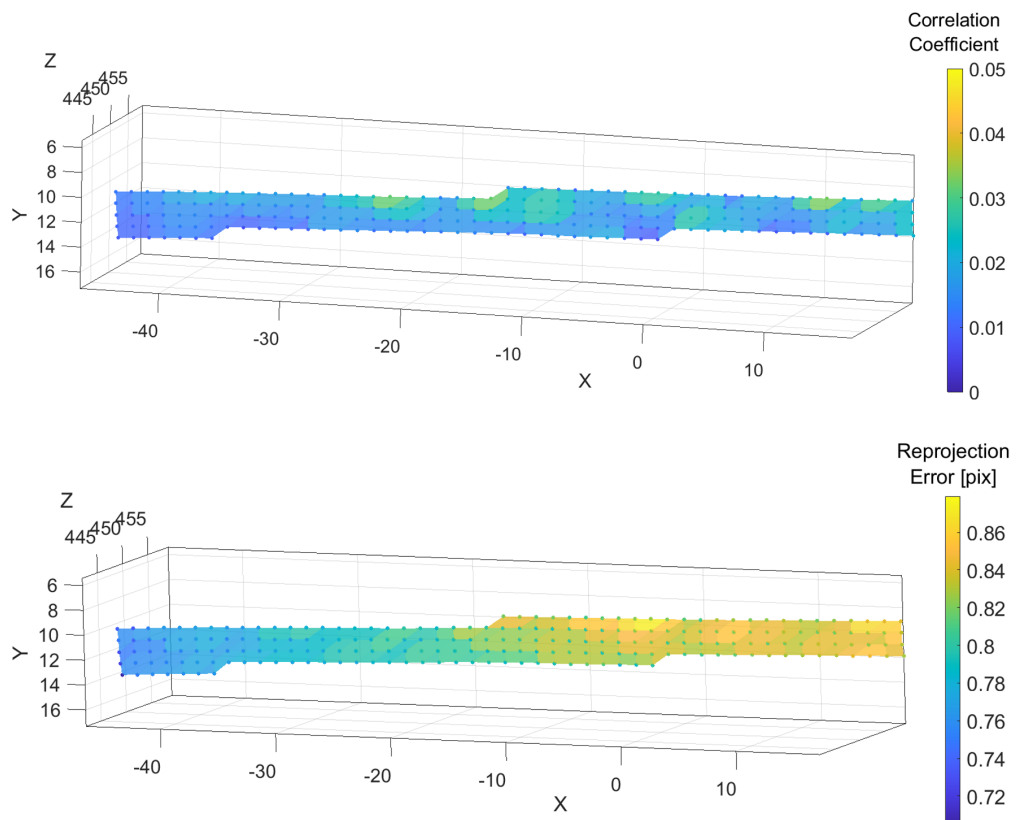


**Figure 4:** Step 3 results: 3D reconstruction and animated plots of the correlation coefficients and the reprojection errors.

#### 107     Step 4: Post processing

108     The 3D coordinates calculated in Step 3 are used in this step to derive the full-field displacement,  
 109     deformation, and strain maps. The displacements are calculated for each point, and the  
 110     deformations and strains are calculated for each triangular element, using the Cosserat point  
 111     element method (Solav et al., 2014, 2016; Solav, Camomilla, et al., 2017; Solav, Meric, et al.,  
 112     2017). Detailed information on the post processing methods can be found in the MultiDIC  
 113     paper (Solav et al., 2018). In short, for each triangular element, the position vectors of its  
 114     vertices are used to calculate the deformation gradient tensor  $\mathbf{F}$ , from which the right and  
 115     left Cauchy-Green deformation tensors ( $\mathbf{C} = \mathbf{F}^T \mathbf{F}$  and  $\mathbf{B} = \mathbf{F} \mathbf{F}^T$ , respectively) are derived,  
 116     as well as the Green-Lagrangian and Eulerian-Almansi strain tensors ( $\mathbf{E} = 0.5(\mathbf{C} - \mathbf{I})$  and  
 117      $\mathbf{e} = 0.5(\mathbf{I} - \mathbf{B}^{-1})$ , respectively). The principal components and directions of these tensors  
 118     are computed for deriving the principal stretches  $\lambda_i$  and strains  $E_i$  and  $e_i$ , as well as the  
 119     equivalent (Von-Mises) strain, maximal shear strain, and area change.

120     **Figure 5** and **Figure 6** show two example figures, plotting the 3D displacement magnitudes  
 121     overlaid on the images and first and second principal Lagrangian strains (magnitude and  
 122     directions) on the 3D triangular mesh, respectively. Examples of animated GIF files exported  
 123     using DuoDIC can be found in the GitHub repository.

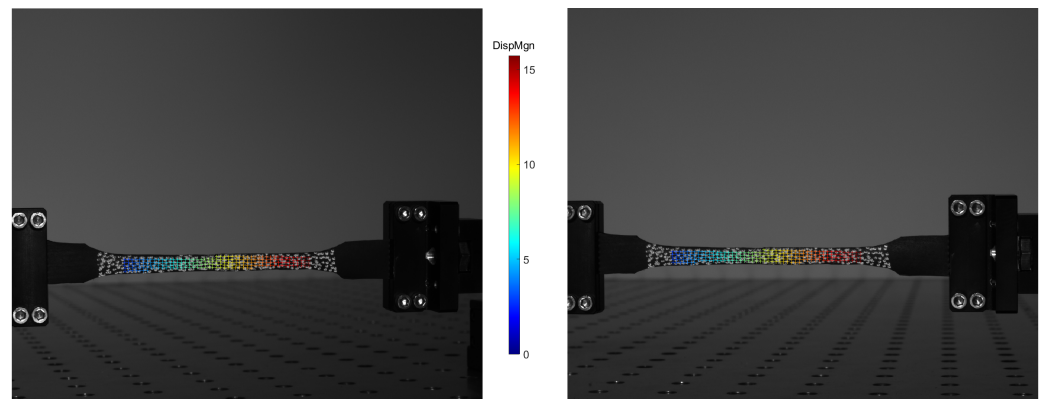


**Figure 5:** Full-field displacement magnitudes (in mm) overlaid on the original images.

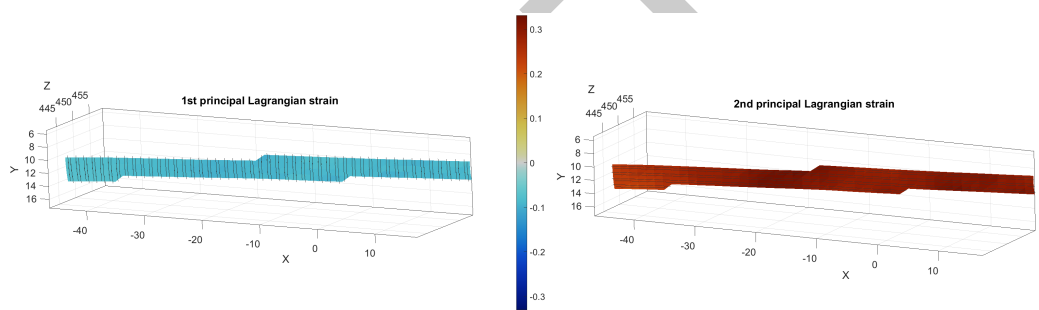


**Figure 6:** First (minimal) and second (maximal) principal strains plotted as 3D surfaces represented by triangular meshes, with face colors depicting the strain magnitude and the black lines depicting the strain direction.

## 124 Validation using a rigid body motion (RBM) test

125 To assess the metrological performance of DuoDIC, we performed a rigid body motion ex-  
 126 periment, whereby a speckled cylinder was translated using a motorized linear translation  
 127 stage (PT1/M-Z8, Thorlabs, USA), in 15 increments of 0.2 mm. simultaneous images were  
 128 captured using the same camera setup described in the previous section. By comparing the  
 129 displacements measured using the translation stage with those computed using DuoDIC, the  
 130 displacement errors were quantified, as shown in [Figure 7](#). In addition, since strain should  
 131 vanish for any RBM, any non-zero strains represent measurement errors. [Figure 8](#) plots the  
 132 strains measured during the RBM translations. The results indicate that for this experimental  
 133 setup, the translations were accurate to within  $(1.3 \pm 1.1) \cdot 10^{-3}$  mm (mean  $\pm$  STD absolute  
 134 translation error) and the strains errors were  $(3.4 \pm 2.3) \cdot 10^{-4}$ .

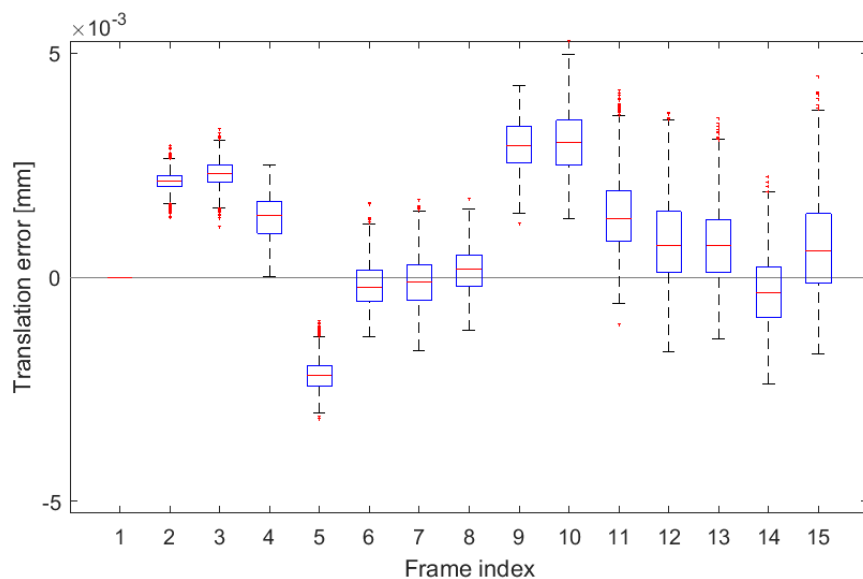


**Figure 7:** Translation errors representing the difference between the translations measured by the translation stage and those computed using DuoDIC. On each box, the central red line indicates the median, the bottom and top edges of the box indicate the 25th and 75th percentiles, the whiskers extend to the most extreme data points not considered outliers, and the outliers are plotted individually using red points

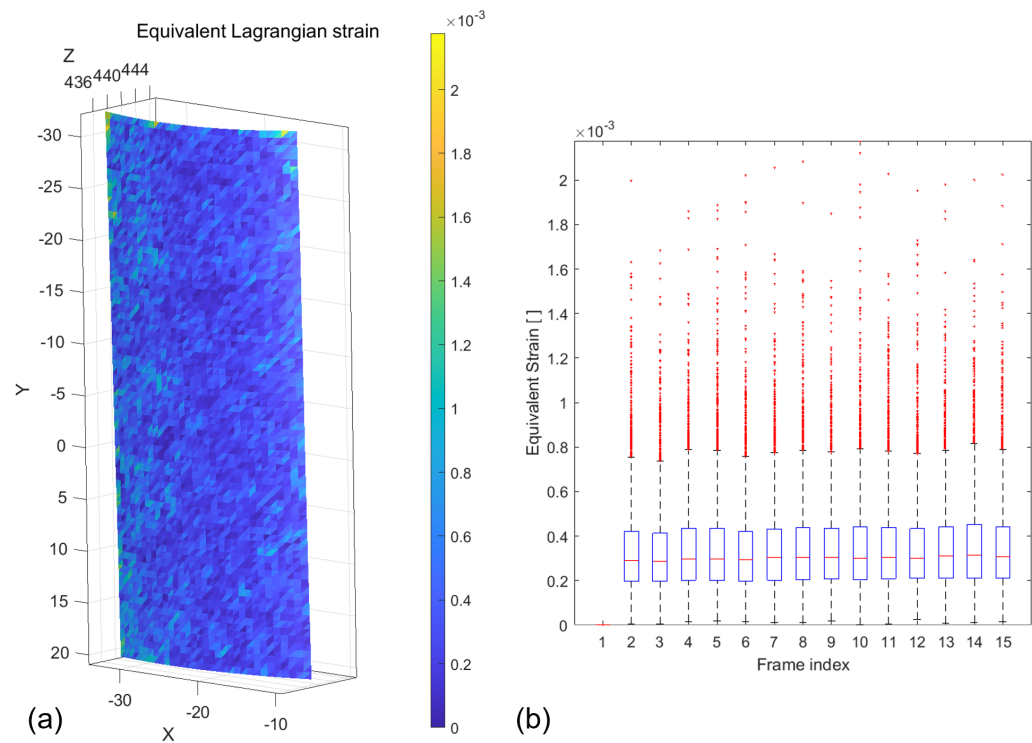


**Figure 8:** Strain values measurements during the RBM test represent the errors in the strain measurement. (a) 3D surface of the cylinder ROI in the last translation step showing the distribution of strains across the surface. (b) Strain results for all the faces measured at each translation step. On each box, the central red line indicates the median, the bottom and top edges of the box indicate the 25th and 75th percentiles, the whiskers extend to the most extreme data points not considered outliers, and the outliers are plotted individually using red points.

## 135 Acknowledgements

136 This project was supported by Dana Solav's Jacques Lewiner Career Advancement Chair.

## 137 References

- 138 Atkinson, D., & Becker, T. H. (2021). Stereo digital image correlation in MATLAB. *Applied Sciences (Switzerland)*, 11(11), 4904. <https://doi.org/10.3390/app11114904>
- 139 Blaber, J., Adair, B., & Antoniou, A. (2015). Ncorr: Open-Source 2D Digital Image Correlation Matlab Software. *Experimental Mechanics*, 55(6), 1105–1122. <https://doi.org/10.1007/s11340-015-0009-1>
- 140 Bouguet, J.-Y. (2013). *Camera Calibration Toolbox for Matlab: Calibration examples*. [http://www.vision.caltech.edu/bouguetj/calib\\_doc/htmls/example.html](http://www.vision.caltech.edu/bouguetj/calib_doc/htmls/example.html)
- 141 Bradski, G., & Kaehler, A. (2008). *Learning OpenCV* (First Edit). O'Reilly Media, Inc.
- 142 ISBN: 978-0-596-51613-0
- 143 Heikkila, J., & Silven, O. (1997). A four-step camera calibration procedure with implicit image correction. *Proceedings of IEEE Computer Society Conference on Computer Vision and Pattern Recognition*, 1106–1112. <https://doi.org/10.1109/CVPR.1997.609468>

- 150 Moerman, K. M. (2018). GIBBON: The Geometry and Image-Based Bioengineering add-On.  
151 *The Journal of Open Source Software*, 3(22), 506. <https://doi.org/10.21105/joss.00506>
- 152 Pan, B. (2018). Digital image correlation for surface deformation measurement: Historical  
153 developments, recent advances and future goals. *Measurement Science and Technology*,  
154 29(8). <https://doi.org/10.1088/1361-6501/aac55b>
- 155 Reu, P. (2015). THE ART AND APPLICATION OF DIC DIC : A Revolution in Experimental  
156 Mechanics. *Experimental Techniques*, 39(Dic), 1–2. <https://onlinelibrary.wiley.com/doi/pdf/10.1111/ext.12173>
- 158 Solav, D., Camomilla, V., Cereatti, A., Barré, A., Aminian, K., & Wolf, A. (2017). Bone  
159 orientation and position estimation errors using Cosserat point elements and least squares  
160 methods: Application to gait. *Journal of Biomechanics*, 62, 110–116. <https://doi.org/10.1016/j.jbiomech.2017.01.026>
- 162 Solav, D., Meric, H., Rubin, M. B., Pradon, D., Lofaso, F., & Wolf, A. (2017). Chest  
163 Wall Kinematics Using Triangular Cosserat Point Elements in Healthy and Neuromuscular  
164 Subjects. *Annals of Biomedical Engineering*, 45(8), 1963–1973. <https://doi.org/10.1007/s10439-017-1840-6>
- 166 Solav, D., Moerman, K. M., Jaeger, A. M., Genovese, K., & Herr, H. M. (2018). MultiDIC:  
167 an Open-Source Toolbox for Multi-View 3D Digital Image Correlation. *IEEE Access*, 6,  
168 30520–30535. <https://doi.org/10.1109/ACCESS.2018.2843725>
- 169 Solav, D., Rubin, M. B. B., Cereatti, A., Camomilla, V., & Wolf, A. (2016). Bone Pose  
170 Estimation in the Presence of Soft Tissue Artifact Using Triangular Cosserat Point Ele-  
171 ments. *Annals of Biomedical Engineering*, 44(4), 1181–1190. <https://doi.org/10.1007/s10439-015-1384-6>
- 173 Solav, D., Rubin, M. B. B., & Wolf, A. (2014). Soft Tissue Artifact compensation using Tri-  
174 angular Cosserat Point Elements (TCPEs). *International Journal of Engineering Science*,  
175 85, 1–9. <https://doi.org/10.1016/j.ijengsci.2014.07.001>
- 176 Sutton, M. A., Matta, F., Rizos, D., Ghorbani, R., Rajan, S., Mollenhauer, D. H., Schreier, H.  
177 W., & Lasprilla, A. O. (2017). Recent Progress in Digital Image Correlation: Background  
178 and Developments since the 2013 W M Murray Lecture. *Experimental Mechanics*, 57(1),  
179 1–30. <https://doi.org/10.1007/s11340-016-0233-3>
- 180 Turner, D. (2015). *Digital Image Correlation Engine (DICe) Reference Manual*. Sandia  
181 Report. <https://github.com/dicengine/>
- 182 Zhang, Z. (2000). A Flexible New Technique for Camera Calibration. *IEEE Transactions on*  
183 *Pattern Analysis and Machine Intelligence*, 22(11), 1330–1334. <https://doi.org/10.1109/34.888718>